NJC

ROYAL SOCIETY OF CHEMISTRY

PAPER

View Article Online
View Journal

Cite this: DOI: 10.1039/d6nj00220j

Design and evaluation of a Bi_2O_3/g-C_3N_4/$NiMnO_3$ composite for dye degradation under simulated solar light and charge storage

Rasmirekha Pattanaik, Rishabh Kamal, Debapriya Pradhan and Suresh Kumar Dash *

A ternary photocatalyst, Bi_2O_3/g-C_3N_4/$NiMnO_3$, was synthesized *via* simple calcination, where $NiMnO_3$ incorporation into the Bi_2O_3/g-C_3N_4 matrix formed a dual S-scheme heterojunction with g-C_3N_4 acting as an electron mediator between Bi_2O_3 and $NiMnO_3$. This configuration enhanced charge transfer, promoted electron–hole separation, and improved redox activity, as confirmed by structural, morphological, and optical characterization. The Bi_2O_3/g-C_3N_4/$NiMnO_3$ composite exhibited significantly improved photocatalytic activity toward the degradation of mixed organic dyes, cationic crystal violet (CV) and anionic Congo red (CR), under natural solar light irradiation. The optimized catalyst achieved approximately 99% degradation of crystal violet (CV), 94% of Congo red (CR), and 92% degradation of mixed dyes within 90 min under ambient conditions, using 40 mg of catalyst in 40 mL of dye solution at standard temperature and pressure. The pH values were adjusted to pH 7 for crystal violet (CV), pH 3 for Congo red (CR), and pH 6 for the mixed dye solution, based on the optimal stability and adsorption behaviour of the respective dyes in aqueous media. The photocatalytic degradation followed pseudo-first-order kinetics (R^2 = 0.98) for the mixed dye, indicating efficient and reproducible reaction behaviour. Photoluminescence (PL) spectra confirmed the suppressed recombination of photo-induced charge carriers, consistent with the proposed dual S-scheme charge transfer mechanism. Radical scavenging identified $^{\bullet}OH$ and $^{\bullet}O_2^-$ as key reactive species, and the photocatalyst retained good stability and reusability after four cycles. Electrochemical analysis verified efficient charge transport and stable semiconducting behaviour.

Received 20th January 2026,
Accepted 18th March 2026

DOI: 10.1039/d6nj00220j

rsc.li/njc

1. Introduction

The generation of organic wastewater has increased significantly due to the rapid expansion of industrial and agricultural activities.[1] Accelerated industrialization has led to severe water pollution, with an estimated 10–15% of organic dyes being discharged into lakes, rivers, and groundwater, posing carcinogenic and mutagenic risks to human health.[2]

Conventional wastewater treatment methods, such as adsorption, coagulation, flocculation, and biological degradation, suffer from inherent limitations including incomplete mineralization, secondary pollution, and high operational costs. In contrast, photocatalytic processes represent sustainable and eco-friendly alternatives that utilize light energy to drive reactions such as water splitting and pollutant degradation through photon absorption, charge separation, carrier migration, and surface redox reactions.[3,4]

In recent years, numerous semiconductor photocatalysts, including TiO_2,[4] ZnO,[5] Ag_2CO_3,[6] g-C_3N_4,[7] Bi_2O_3[8] and MoS_2,[9] have been extensively investigated. However, single-component semiconductors often exhibit limited visible-light activity due to wide band gaps and rapid recombination of photogenerated charge carriers.[10]

Among these materials, perovskite-type oxides (ABO_3), containing alkaline earth or rare-earth metals at the A-site and transition metals at the B-site, have attracted considerable attention owing to their favourable electronic structures and photocatalytic properties. Perovskites such as $LaFeO_3$, $NiMnO_3$, $BaTiO_3$, $BiFeO_3$, and $SrTiO_3$ have been widely studied for photocatalytic applications.[11,12]

Among these, nickel manganese oxide ($NiMnO_3$), a mixed-metal perovskite oxide, is notable for its low cost, good specific capacity, and high electrical conductivity, making it an attractive candidate for energy-storage applications.[13] $NiMnO_3$ exhibits excellent chemical and physical stability and is synthesized from abundant and nontoxic elements, rendering it environmentally benign and sustainable. Consequently, $NiMnO_3$ has

Department of Chemistry, ITER, Siksha 'O' Anusandhan (Deemed to be University), Bhubaneswar, Odisha 751030, India. E-mail: sureshdash@soa.ac.in

been explored for diverse applications, including photocatalysis, water splitting for hydrogen production, electrocatalysis, and supercapacitors.[14,15] The synergistic redox activity of Ni^{3+}/Ni^{2+} and Mn^{4+}/Mn^{3+} ions enhances charge transfer and catalytic efficiency while mitigating the limitations of single-metal oxides. Nevertheless, the wide bandgap of $NiMnO_3$ (3.0–3.5 eV) restricts its photoresponse primarily to the UV region, resulting in poor visible-light utilization and limited photocatalytic efficiency.[16,17] Therefore, bandgap engineering is essential to improve its solar-light activity.

To overcome these limitations, coupling $NiMnO_3$ with narrow bandgap semiconductors such as Bi_2O_3 and graphitic carbon nitride (g-C_3N_4) provides a promising strategy for constructing efficient heterostructures with enhanced light absorption and improved charge separation. Bi_2O_3 is a nontoxic and chemically stable semiconductor with a relatively narrow bandgap (2.1–2.8 eV), high surface area, strong oxidation ability of valence-band holes (+3.13 V *vs.* NHE), and excellent visible-light activity. These properties make Bi_2O_3 suitable for applications in photocatalysis, sensors, fuel cells, coatings, and gas detection, although its performance is limited by rapid charge recombination.[18,19] Similarly, g-C_3N_4 is a low-cost, metal-free, and environmentally friendly photocatalyst that exhibits visible-light activity and has been applied in pollutant degradation, water splitting, CO_2 reduction, and organic synthesis. However, its photocatalytic efficiency is constrained by low surface area, limited light absorption, and fast charge recombination, which can be mitigated through heterostructure engineering or elemental modification.[20]

To achieve synergistic functionality, heterostructure engineering has emerged as a promising approach to combine the complementary advantages of individual semiconductors. When Bi_2O_3, g-C_3N_4, and $NiMnO_3$ are integrated, a ternary heterojunction is formed, which not only facilitates efficient charge migration but also broadens the light absorption spectrum across UV-visible regions. The combination of these materials enhances the redox potential, suppresses charge recombination, and provides abundant active sites for surface reactions.

Heterostructure construction has emerged as an effective approach to integrate the complementary advantages of individual semiconductors. The integration of Bi_2O_3, g-C_3N_4, and $NiMnO_3$ into a ternary heterojunction facilitates efficient interfacial charge transfer, broadens the solar-light absorption range, suppresses electron–hole recombination, and enhances redox activity by providing abundant surface-active sites. Various synthesis methods have been reported for $NiMnO_3$-based heterostructures, including co-precipitation,[21] thermal treatment,[22] the sol–gel auto combustion route,[23] hydrothermal,[24] microwave-asisted,[25] and precipitation.[26] Previous studies on $NiMnO_3$-based systems have primarily focused on binary composites, such as mixed dyes. Krishna Chandar Nagamuthu Rajaa *et al.* developed a $NiMnO_3/NiMn_2O_4$–$Ti_3C_2T_x$ MXene (20 wt%) photocatalyst that can photodegrade 90%, 72%, and 100% of rhodamine B (RhB), methyl orange (MO), and methylene blue (MB) after 50 min under visible light illumination.[27] Krishna Chandar Nagamuthu Raja *et al.* and his colleagues created $NiMnO_3/NiMn_2O_4$–graphene nanocomposites and they found that the $NiMnO_3/NiMn_2O_4$–graphene nanocomposite demonstrated superior photocatalytic performance higher than that of $NiMnO_3$, as it degrades methylene blue (MB) dye with 100% efficiency in 30 min under visible light absorption.[28]

Beyond photocatalysis, $NiMnO_3$ and its composites have gained increasing attention for supercapacitor applications due to the pseudo capacitive behaviour arising from the reversible redox reactions of Ni and Mn ions. The incorporation of Bi_2O_3 and g-C_3N_4 further improves electron and ion transport, increases the electrochemically active surface area, and stabilizes the electrode structure, enabling high-performance energy-storage devices. Although perovskite oxides, Bi-based oxides, and g-C_3N_4 have been widely explored individually or in binary combinations, reports on their rational integration into a Bi_2O_3/g-C_3N_4/$NiMnO_3$ ternary heterostructure remain scarce. In particular, $NiMnO_3$-based systems have largely been limited to binary composites and single-function studies. In this work, the ternary heterostructure enables effective bandgap engineering, enhanced solar-light absorption, and accelerated interfacial charge transfer, leading to suppressed charge recombination. Moreover, this study demonstrates the dual functionality of the synthesized material for solar light-driven mixed dye degradation and supercapacitor energy storage, supported by systematic parameter optimization and density functional theory (DFT)-assisted mechanistic insights.

To the best of our knowledge, the photocatalytic performance of a Bi_2O_3/g-C_3N_4/$NiMnO_3$ ternary nanocomposite for the degradation of mixed organic dyes under solar illumination has not been previously reported. Accordingly, a novel ternary nanocomposite was synthesized using a simple and effective approach, and its structural, optical, morphological, and electrochemical properties were thoroughly characterized using XRD, Raman, FTIR, UV-vis spectroscopy, FESEM–EDX, BET surface area analysis, TEM, photoluminescence, and cyclic voltammetry. The photocatalytic activity was evaluated using a mixture of Congo red and crystal violet dyes, and the degradation mechanism was systematically elucidated, while the electrochemical performance confirmed its potential as a high-performance supercapacitor electrode.

2. Experimental details

2.1 Chemicals

The chemicals used in this study include nickel nitrate hexahydrate ($Ni(NO_3)_2{\cdot}6H_2O$, Merck, 99.9% purity), manganese nitrate hexahydrate ($Mn(NO_3)_2{\cdot}6H_2O$, Merck, 99.9% purity), bismuth nitrate pentahydrate ($Bi(NO_3)_2{\cdot}5H_2O$, Merck, 99.9% purity), sodium sulfate (Na_2SO_4, Merck, 99.9% purity), sodium bicarbonate ($NaHCO_3$, Merck, 99.9% purity), sodium hydroxide (NaOH, Merck, 99.9% purity), melamine, and crystal violet and Congo red dye (Merck, 99% purity). The solutions were prepared using deionized, double-distilled water (DI) and

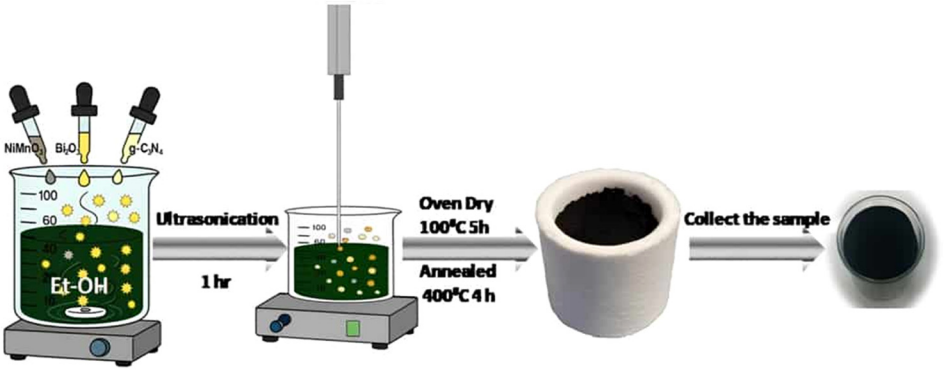

Scheme 1 Schematic diagram of the synthesis of Bi_2O_3/g-C_3N_4/$NiMnO_3$ by the co-precipitation method.

analytical-grade ethanol (C_2H_5OH, Fisher Chem., 99%). All other reagents used in both the synthesis and experimental procedures were of laboratory-grade purity and quality.

2.2 Synthesis of the Bi_2O_3/g-C_3N_4/$NiMnO_3$ and their characterization

The Bi_2O_3/g-C_3N_4/$NiMnO_3$ composite was produced by a calcination method (Scheme 1). At first, a fixed amount of as-prepared $NiMnO_3$,[29] Bi_2O_3[30] and g-C3N4[31] powders was taken in a molar ratio of 4 : 3 : 2 and dispersed in a mixture of 50 mL ethanol and distilled water. The suspension was subjected to ultrasonication for 1 h to obtain a homogeneous mixture. The resulting slurry was dried in an oven at 100 °C for 5 h, followed by annealing at 400 °C for 4 h in an electric muffle furnace (JSMF-30T). The final product was denoted as BGN, representing the Bi_2O_3/g-C_3N_4/$NiMnO_3$ composite.

2.3 Material characterization

The crystallographic structure of the synthesized materials was analyzed by X-ray diffraction (XRD) using a PANalytical diffractometer (PW 1830, Philips, Japan) with Cu-Kα radiation (λ = 1.5406 Å), operated at 40 kV and 30 mA, over a 2θ range of 10–80° with a step size of 0.02°, and phases were identified using standard JCPDS files. Elemental composition and distribution were examined by energy-dispersive X-ray spectroscopy (EDS) attached to a field-emission scanning electron microscope (FESEM, ZEISS SUPRA 55), which was also used to study the surface morphology at accelerating voltages of 5–15 kV, while detailed microstructural and lattice information was obtained by high-resolution transmission electron microscopy (HR-TEM, JEOL JEM-2100) operated at 200 kV. Functional groups and bond vibrations were identified using Fourier-transform infrared (FTIR) spectroscopy (PerkinElmer Spectrum, version 10.4.3) in the range of 400–4000 cm^{-1} with a resolution of 4 cm^{-1}, and Raman spectra were recorded at 312 K using a Renishaw (UK) spectrometer with a 785 nm diode laser. Optical properties were evaluated by UV-visible diffuse reflectance spectroscopy (UV-DRS, PerkinElmer Lambda 365), and band gap energies were estimated using the Kubelka–Munk function and Tauc plots, while photoluminescence spectroscopy was employed to assess charge-carrier recombination behaviour. Electrochemical characteristics were studied by cyclic voltammetry using a PGSTAT 204 workstation in a three-electrode configuration, and the specific surface area and pore size distribution were determined by Brunauer Emmett Teller (BET) nitrogen adsorption–desorption analysis using a Quantachrome Instruments analyzer (v11.05) after prior degassing of the samples. Dye concentrations before and after photocatalytic degradation were measured using a UV-vis spectrophotometer (Systronics 2202), and surface chemical composition and oxidation states were analyzed by X-ray photoelectron spectroscopy (XPS, ESCA+ Omicron Nano Technology) using Al Kα radiation with binding energies calibrated to the C 1s peak at 284.8 eV.

2.4 Photocatalytic study setup

The photocatalytic performance of the synthesized nanocomposites was evaluated through the degradation of crystal violet (CV), Congo red (CR), and their mixed dye solution under natural sunlight irradiation. In a typical experiment, 25 mL of aqueous dye solution (crystal violet (CV): λ_{max} = 590 nm, Congo red (CR): λ_{max} = 497 nm, and mixed dye: λ_{max} = 530 nm) with a fixed initial concentration was mixed with 0.04 g of the photocatalyst in a 250 mL beaker. Prior to light irradiation, the suspension was magnetically stirred in the dark for 30 min to establish adsorption–desorption equilibrium; dark control experiments were conducted under identical conditions of dye concentration, catalyst dosage, volume, and pH, but without light exposure. After equilibration, the reaction mixture was exposed to sunlight to initiate photocatalysis. At regular time intervals, 2.5 mL aliquots were withdrawn, centrifuged to remove the catalyst, and the residual dye concentration was determined using a UV-vis spectrophotometer. The photocatalytic degradation efficiency was calculated using the dye concentration at time t (C) and the equilibrium concentration at time t (C_0).

$$\%\,\text{Degradation} = 1 - \frac{C}{C_0} \times 100 \quad (1)$$

2.5 Scavenger test

To identify the key active species in the degradation process, scavenger tests were performed on the crystal violet (CV), Congo red (CR) and mix dye solution before the reaction. IPA, EDTA,

and BQ were used to trap hydroxyl radicals ($^{\bullet}OH$), superoxide radicals ($^{\bullet}O_2^-$), and holes (h^+), respectively. This trapping analysis helped evaluate the photocatalytic activity under consistent conditions.

2.6 Theoretical analysis using density functional theory (DFT)

Density functional theory (DFT) calculations were performed using ORCA 5.0 with the B3LYP/g hybrid functional and def2/J basis set to optimize the molecular geometries of the mixed dye (Congo red (CR) + crystal violet (CV)) and Bi_2O_3/g-C_3N_4/$NiMnO_3$. The ground-state structures and frontier molecular orbitals (HOMO and LUMO) were visualized using Avogadro 1.2.0. The interaction energy between the mixed dye (Congo red (CR) + crystal violet (CV)) and Bi_2O_3/g-C_3N_4/$NiMnO_3$ (E_{inter}) was calculated at the same level of theory using:

$$E_{inter} = E_{mix\,dye-Bi_2O_3/g\text{-}C_3N_4/NiMnO_3} - (E_{mix\,dye} + E_{Bi_2O_3/g\text{-}C_3N_4/NiMnO_3}) \quad (2)$$

where $E_{mix\,dye-Bi_2O_3/g\text{-}C_3N_4/NiMnO_3}$, $E_{mix\text{-}dye}$ and $E_{Bi_2O_3/g\text{-}C_3N_4/NiMnO_3}$ correspond to the total energies of the mixed dye–Bi_2O_3/g-C_3N_4/$NiMnO_3$ complex, isolated mixed dye, and isolated Bi_2O_3/g-C_3N_4/$NiMnO_3$ respectively.

3. Results and discussion

3.1 Structural analysis

The XRD patterns of the synthesized nanocomposites are presented in Fig. 1, illustrating the crystalline phases of each component. Nickel manganese oxide belongs to the perovskite oxide family having JCPDS No: 75-2089, which also indicates that the pure phase $NiMnO_3$ has been successfully prepared. The $NiMnO_3$ crystal structure is constructed by NiO_6 octahedra and MnO_6 octahedra. They are linked together by sharing oxygen vertices.[32,33] Strong diffraction peaks aligned with the (012), (104), (110), (113), (024), (116), (214), and (300) crystal planes of $NiMnO_3$ were detected at 24.2°, 33.4°, 36.9°, 41.1°, 50.9°, 64.6°, and 65.2°.[34] The XRD pattern of Bi_2O_3 shows labelled peaks without other detectable phases. Peaks at 28.6°(201), 31.2°(002), 32.2°(220), 46.7°(222), 47.4°(400), and 54.5°(203) correspond to β-Bi_2O_3 (JCPDS No. 27-0050), while the (201) plane also indicates γ-Bi_2O_3, revealing a mixed-phase composition dominated by β-Bi_2O_3.[35,36] g-C_3N_4 has a modest peak at 12.9° associated with the (100) planes of tris-triazine units of JCPDS 87-1526 and a significant peak at 27.7° relating to the (002) planes of layered structures.[37,38] The absence of impurity peaks in the XRD pattern confirms the successful fabrication of the BGN heterojunction shown in Fig. 1 and indicates no reaction between the individual semiconductors.[39] The reflected crystallographic parameters of the synthesized materials are enlisted in Table 1.

According to the Scherrer equation, crystallite size,

$$\mathcal{D}_c = \frac{K\lambda}{\beta \cos\theta} \quad (3)$$

where λ is the wavelength of the Cu source, β is the full width at half maximum (in radians) and θ is the diffraction angle (in degrees). The calculated crystallite size of BGN is 33.74 nm. The significantly smaller crystallite size compared to the pure form of the catalysts supported the assumption that loading Bi_2O_3 and g-C_3N_4 effectively surpasses the grain growth of $NiMnO_3$, leading to the formation of smaller crystalline particles.[40]

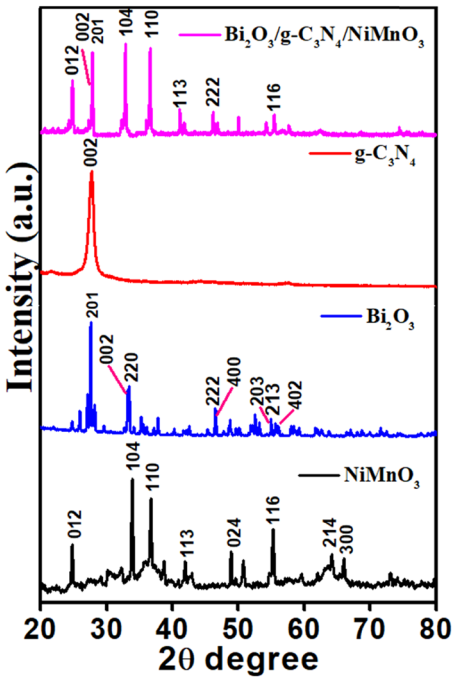

Fig. 1 XRD patterns of $NiMnO_3$, Bi_2O_3, g-C_3N_4, and the Bi_2O_3/g-C_3N_4/$NiMnO_3$ composite, confirming the successful formation and coexistence of all phases in the ternary heterostructure.

It is important to note that $NiMnO_3$ intrinsically forms small crystallites, whereas Bi_2O_3 and g-C_3N_4 typically have larger particle sizes. In the BGN composite, the small average crystallite size primarily reflects the intrinsic dimensions of $NiMnO_3$ and its dispersion within the Bi_2O_3/g-C_3N_4 matrices, which may hinder local agglomeration without implying direct "grain-size reduction" by the other components. This clarification provides a more accurate description of the interactions and structural features within the heterostructure.

3.2 Functional group analysis

In Fig. 2, the FTIR spectroscopy of the produced $NiMnO_3$ nanoparticles was performed to identify functional groups and investigate their chemical structure. The spectrum showed absorption bands below 1000 cm^{-1} at 497 cm^{-1} and 585 cm^{-1}, corresponding to the Ni–O and Mn–O metal–oxygen vibrations. The bands at 1635 cm^{-1} and 3413 cm^{-1} were attributed to the H–O–H bending and O–H stretching vibrations of adsorbed water.[41] For Bi_2O_3, the BiO_6 octahedron peaks at 424 cm^{-1} and 503 cm^{-1} represented Bi–O bond vibrations, while the Bi–O–Bi stretching vibration appeared at 845 cm^{-1}. The O–H stretching vibration of adsorbed water was detected at 3425 cm^{-1}, and the characteristic nitrate group was observed at 1380 cm^{-1}.[42] The weak band observed near 1380 cm^{-1} is attributed to trace surface-adsorbed nitrate species originating from the bismuth

Table 1 Crystallographic parameters of the synthesized nanoparticles

Serial no	Sample name	Crystal phase	Space group	Crystal size (nm)	Lattice parameters
1	$NiMnO_3$	Rhombohedral	R3 spatial symmetry	35.43	a = 4.89 Å, b = 4.89 Å, and c = 13.60 Å
2	Bi_2O_3	Tetragonal	$P\bar{4}2_1c$	46.98	$a = b$ = 7.749 Å, c = 5.632 Å
3	g-C_3N_4	Hexagonal	$P6_3cm$ (185)	46.87	$a = b = c$ = 0.67 Å

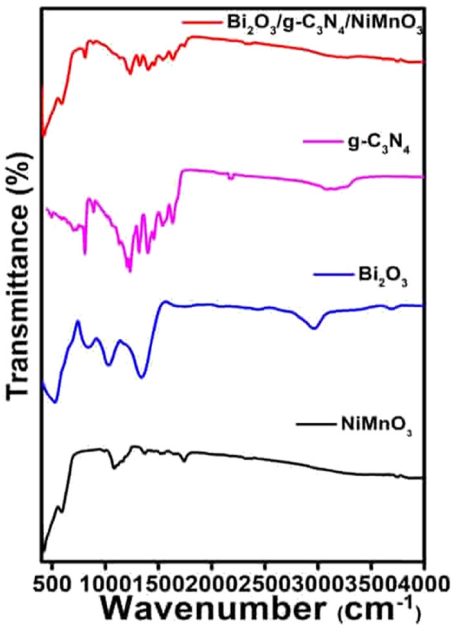

Fig. 2 FTIR spectra of $NiMnO_3$, Bi_2O_3, g-C_3N_4, and Bi_2O_3/g-C_3N_4/$NiMnO_3$, confirming the presence of functional groups from all components in the composite.

nitrate precursor used during synthesis. Since pure Bi_2O_3 does not intrinsically contain nitrate groups in its crystal structure, this peak arises from residual surface species rather than structural nitrate. In g-C_3N_4, the peak at 801 cm^{-1} was linked to the breathing mode of the triazine units, while strong bands in the 1200–1650 cm^{-1} range corresponded to CN heterocycle stretching. NH stretching vibrations were observed around 3000 cm^{-1}.[43] In the ternary composite of BGN, small shifts in the absorption peaks at 589 cm^{-1}, 1375 cm^{-1}, and 805 cm^{-1} are observed, linked to Mn–O and N–O stretching vibrations. The signals at 497 cm^{-1} and 503 cm^{-1} correspond to Ni–O and Bi–O–Bi stretching vibrations, indicating BGN photocatalyst formation. The O–H stretching vibration signals are broader and weaker in BGN, with O–H groups playing a key role in photocatalytic activity by trapping holes to form $OH^{\bullet}$ radicals, reducing electron–hole recombination and enhancing the photocatalytic process.[44]

3.3 Morphological analysis

3.3.1 Scanning electron microscopy. The morphology of the metal oxides observed by field emission scanning electron microscopy (FE-SEM) is shown in Fig. 3. In Fig. 3(a), $NiMnO_3$ exhibits spherical particles, indicating a *para*-phase structure.[45] In Fig. 3b, Bi_2O_3 exhibits ellipsoidal particles, along with smaller rounded ones and a few larger aggregates, possibly resulting from the fusion of smaller particles.[46] Pure g-C_3N_4 (Fig. 3c) has a two-dimensional nanosheet structure, confirming its successful bulk formation.[47] Fig. 3d shows that in the BGN nanocomposite, g-C_3N_4 nanosheets and ellipsoidal Bi_2O_3 particles are well anchored on spherical $NiMnO_3$. The composite exhibits a uniform morphology with consistent particle size, indicating its potential for applications such as photocatalysis. However, elemental mapping (Fig. 3e and f) indicates that g-C_3N_4 is partially agglomerated rather than perfectly homogeneously distributed, while Ni, Mn, Bi, C, N, and O are overall well dispersed. This non-uniformity of g-C_3N_4 may influence local charge separation and, consequently, photocatalytic activity.

3.3.2 High-resolution transmission electron microscopy. Spherical $NiMnO_3$ particles are evenly distributed and sandwiched between g-C_3N_4 nanosheets and Bi_2O_3 with little aggregation, according to TEM examination (Fig. 4a). Strong interactions can be shown in the magnified pictures, where $NiMnO_3$ is strongly bonded to both g-C_3N_4 and Bi_2O_3. Lattice spacings of 0.14 nm, 0.13 nm, and 0.10 nm are seen in the HRTEM picture (Fig. 4b), which corresponds to g-C_3N_4, Bi_2O_3, and $NiMnO_3$, respectively. These results demonstrate that g-C_3N_4 facilitates effective interfacial charge transfer and supports the Bi_2O_3/$NiMnO_3$ composite. The existence of the nanocomposites is confirmed by the SAED pattern in Fig. 4c. It is anticipated that these interfacial structures would improve photoinduced charge transfer and, consequently, the photocatalytic activity of the composite.[48] In addition to the morphological examination by SEM, the surface area of the nanocomposites was evaluated using BET in S2.

3.4 Optical analysis

UV-Visible spectroscopy (Fig. 5a) reveals that $NiMnO_3$ has an absorption edge at 242 nm, while the BGN composite shows a red-shift into the visible region due to the addition of Bi_2O_3, indicating enhanced light absorption due to strong interfacial interactions. This bathochromic shift suggests improved charge carrier separation and extended lifetimes. The formation of heterojunctions introduces intermediate energy states, facilitating electron transitions and enhancing the material's optical and electronic performance.[49,50] Band gap values derived from Wood and Tauc plots (Fig. 5b) range from 2.7 to 1.8 eV. The band gap of the synthesized photocatalysts was estimated using a Tauc plot based on the classical method.

$$\alpha h\nu = A(h\nu - E_g)^n \quad (4)$$

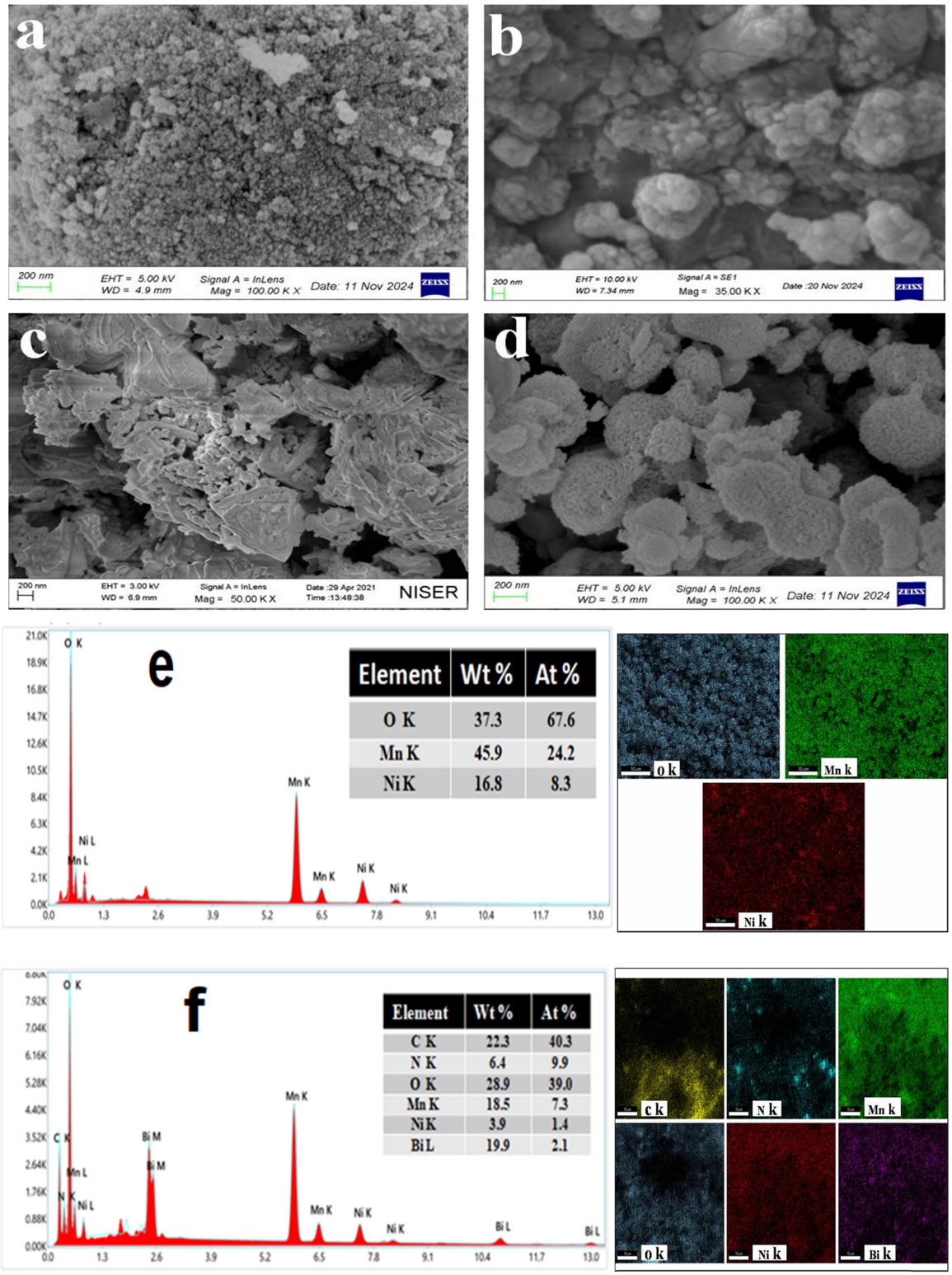

Fig. 3 FESEM images of (a) $NiMnO_3$, (b) Bi_2O_3, (c) g-C_3N_4, and (d) the Bi_2O_3/g-C_3N_4/$NiMnO_3$ nanocomposite; EDX pattern and mapping images of (e) $NiMnO_3$ and (f) BGN nanocomposites, illustrating the surface morphology and microstructural features of the individual components and the ternary heterostructure.

The absorption coefficient (α), band gap energy (E_g), Planck's constant (h), photon energy ($h\nu$), and proportional constant (A) are related through Tauc's equation, where n equals 0.5 for indirect and 2 for direct band-gap semiconductors. Bi_2O_3 is a p-

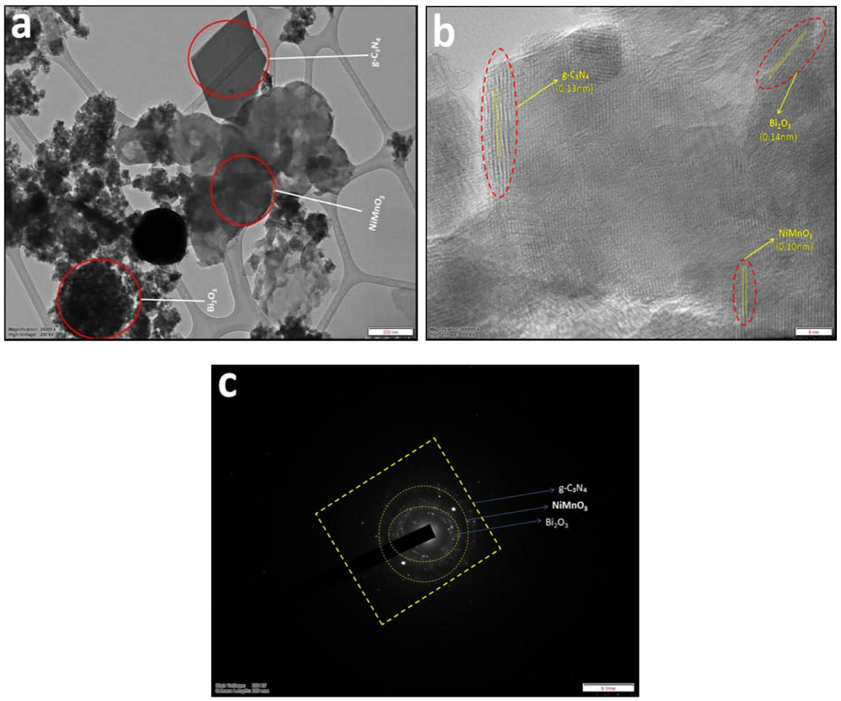

Fig. 4 TEM analyses of the Bi_2O_3/g-C_3N_4/$NiMnO_3$ (BGN) ternary nanocomposite: (a) magnified TEM image, (b) high-resolution TEM (HR-TEM) image showing lattice fringes, and (c) selected area electron diffraction (SAED) pattern confirming the polycrystalline nature.

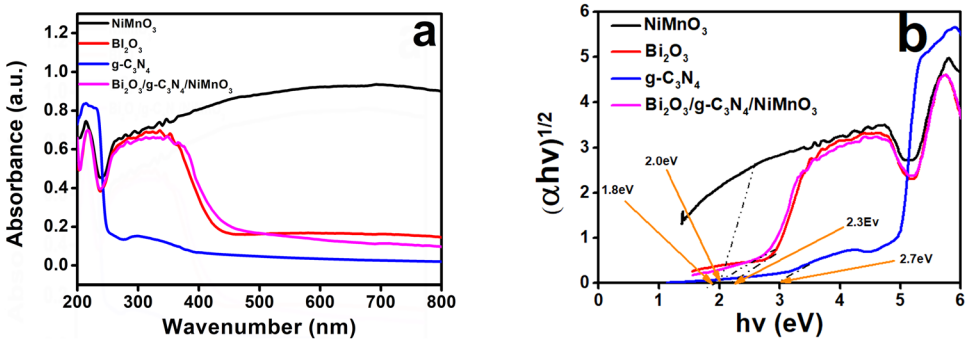

Fig. 5 (a) UV-Vis absorption spectra and (b) Tauc plots of $NiMnO_3$, Bi_2O_3, g-C_3N_4, and the Bi_2O_3/g-C_3N_4/$NiMnO_3$ nanocomposite, illustrating enhanced visible light absorption and reduced band gap in the ternary heterojunction.

type semiconductor and g-C_3N_4 is an n-type semiconductor, while $NiMnO_3$ is a p-type indirect band-gap semiconductor.

The BGN composite shows the narrowest band gap due to enhanced visible-light absorption from mid-gap energy levels introduced by Bi_2O_3 and g-C_3N_4 doping. Additionally, the conduction and valence band positions of the pristine materials, shown in Table 2, were analyzed for their influence on charge separation across heterojunctions. The band-edge positions of the nanocomposites were calculated using standard equations.

$$E_{VB} = X - E_0 + 0.5E_g \quad (5)$$

$$E_{CB} = E_{VB} - E_g \quad (6)$$

Table 2 Values of calculated E_{CB} and E_{VB} for $NiMnO_3$, g-C_3N_4, and Bi_2O_3

Semiconductor	Absolute electronegativity (X)	E_{CB} (eV)	E_{VB} (eV)	E_g (eV)
$NiMnO_3$	3.1 eV	0.5	2.3	1.8
g-C_3N_4	4.25 eV	−1.1	1.6	2.7
Bi_2O_3	3.05 eV	0.3	2.6	2.3
Bi_2O_3/g-C_3N_4/$NiMnO_3$	7.03 eV	1.53	3.53	2.0

The valence band edge potential (E_{VB}) is calculated using the semiconductor's electronegativity (X), which is the geometric mean of its constituent atoms' electronegativities. E_0 represents the free electron energy on the hydrogen scale (~4.5 eV).

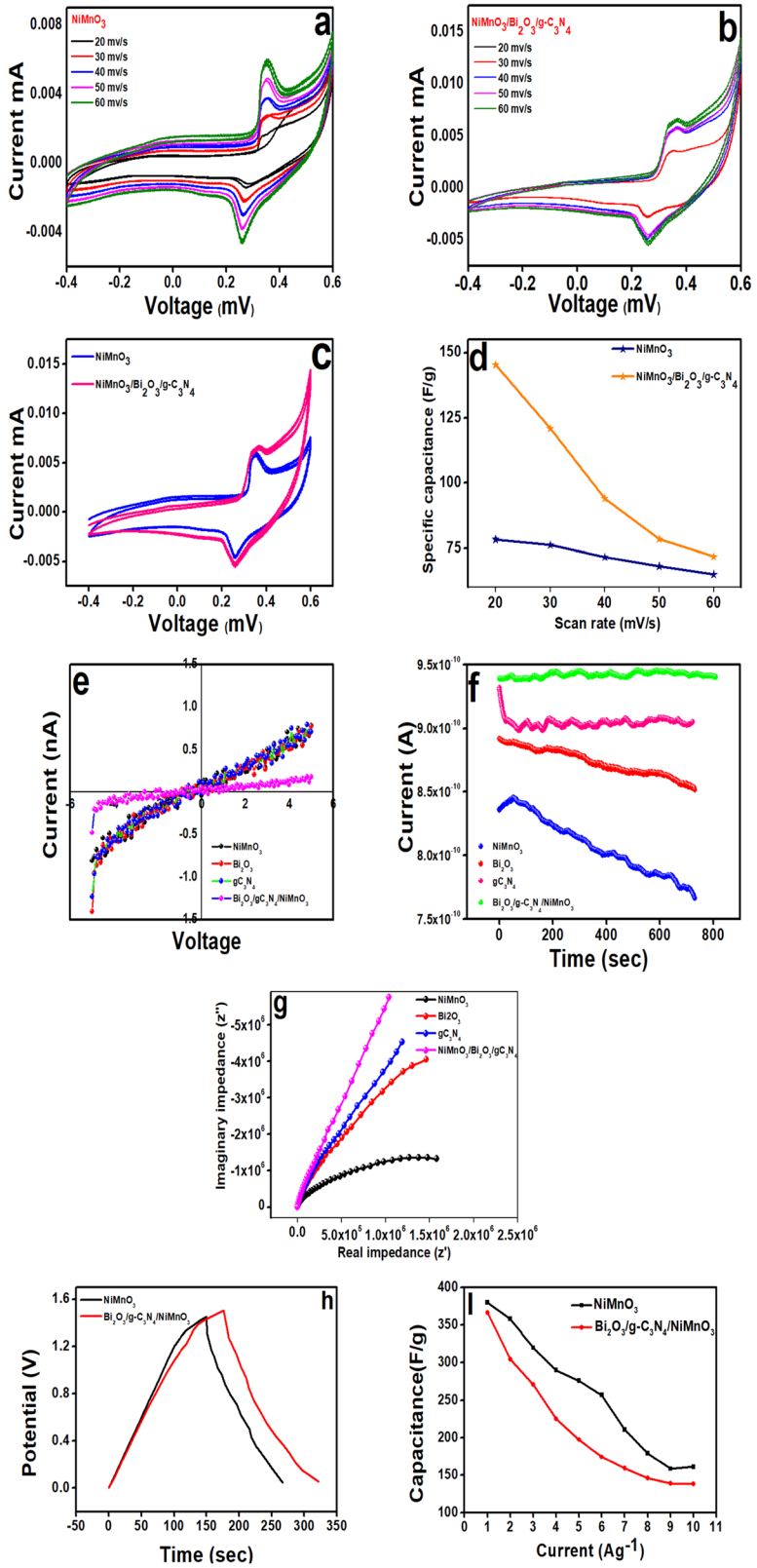

Fig. 6 Electrochemical analysis of $NiMnO_3$ and the Bi_2O_3/g-C_3N_4/$NiMnO_3$ (BGN) nanocomposite: (a) cyclic voltammetry (CV) curves of $NiMnO_3$ at different scan rates, (b) cyclic voltammetry (CV) curves of BGN at different scan rates, (c) comparative cyclic voltammetry (CV) curves of $NiMnO_3$ and Bi_2O_3/g-C_3N_4/$NiMnO_3$ at 50 mV s^{-1}, and (d) variation of specific capacitance with scan rate for both electrodes, (e) *I*–*V* characteristics, (f) *I*–*t* response under light illumination, (g) Nyquist plot from electrochemical impedance spectroscopy (EIS) showing charge transfer resistance, (h) galvanostatic charge discharge (GCD) curves of $NiMnO_3$ and the BGN composite, and (i) variation of specific capacitance with current density for both electrodes.

3.5 Electrochemical analysis

3.5.1 Cyclic voltammetry (CV) and measurement of specific capacitances. The electrochemical performance of $NiMnO_3$ and Bi_2O_3/g-C_3N_4/$NiMnO_3$ was evaluated through cyclic voltammetry (CV) and specific capacitance analysis, as shown in the provided image. Fig. 6a and b depict the cyclic voltammetry (CV) curves of pure $NiMnO_3$ and the ternary Bi_2O_3/g-C_3N_4/$NiMnO_3$ composite at various scan rates (20–60 mV s^{-1}). While both materials exhibit redox peaks indicative of pseudo capacitive behaviour, the ternary composite shows significantly higher current responses, suggesting enhanced charge storage capacity and improved electrochemical activity.[51,52] In Fig. 6c, the direct comparison of both materials at the same scan rate reveals that Bi_2O_3/g-C_3N_4/$NiMnO_3$ has a much larger cyclic voltammetry (CV) area, confirming superior capacitive performance due to the synergistic effect of the incorporated Bi_2O_3 and g-C_3N_4. Furthermore, Fig. 6d shows that the specific capacitance of the composite is notably higher than that of $NiMnO_3$ alone, reaching up to $\sim$150 F g^{-1} at 20 mV s^{-1}, and gradually decreasing with increased scan rate due to diffusion limitations. Overall, the Bi_2O_3/g-C_3N_4/$NiMnO_3$ nanocomposite demonstrates excellent potential for high-performance supercapacitor applications.

3.5.2 Electrochemical impedance studies (EIS). Fig. 6e shows the current–voltage (*I–V*) characteristics of $NiMnO_3$, Bi_2O_3, g-C_3N_4, and the Bi_2O_3/g-C_3N_4/$NiMnO_3$ composite. All samples exhibit nearly linear and symmetric *I–V* curves, indicating ohmic contact between the electrode and electrolyte. The ternary composite displays a comparatively higher current response, suggesting facilitated charge transport across the heterointerfaces.

The photocurrent–time (*I–t*) responses recorded under continuous illumination are shown in Fig. 6f. The ternary composite exhibits the highest photocurrent density with relatively stable behaviour over the measurement duration, indicating efficient generation and transport of photoinduced charge carriers. Although a gradual decay is observed for all samples, the composite maintains a higher photocurrent level than the individual components, reflecting improved charge separation efficiency.

Nyquist plots obtained from electrochemical impedance spectroscopy are presented in Fig. 6g. The Bi_2O_3/g-C_3N_4/$NiMnO_3$ composite shows a larger impedance response compared to the pristine materials, which can be attributed to enhanced interfacial polarization and charge accumulation at the multiple heterojunction interfaces. This increased impedance is indicative of suppressed charge recombination and effective charge trapping, which is beneficial for photocatalytic and photoelectrochemical processes. Overall, the electrochemical results suggest that the ternary heterostructure promotes efficient photoinduced charge separation rather than simple bulk conductivity enhancement.

3.5.3 Galvanostatic charge/discharge studies (GCD). Fig. 6h shows the galvanostatic charge–discharge (GCD) curves of pristine $NiMnO_3$ (black) and the Bi_2O_3/g-C_3N_4/$NiMnO_3$ composite (red) over 0–1.6 V and 0–50 s. Both electrodes display typical charge–discharge cycles, but the composite exhibits a longer discharge time, indicating higher specific capacitance. The gently sloped plateau suggests pseudo capacitive behaviour from redox reactions. In contrast, $NiMnO_3$ shows a shorter discharge period, reflecting lower energy storage. The enhanced performance of the composite arises from the synergistic interaction between Bi_2O_3, g-C_3N_4, and $NiMnO_3$, improving charge storage.[53]

Fig. 6i shows the variation of specific capacitance with current density for both electrodes. Capacitance decreases with increasing current due to limited ion diffusion, but the Bi_2O_3/g-C_3N_4/$NiMnO_3$ composite maintains higher capacitance and better rate performance than $NiMnO_3$. While $NiMnO_3$ shows higher capacitance at low currents, its cycling stability and rate capability are inferior. The specific capacitance (SC) values of the electrodes were calculated from the galvanostatic charge discharge (GCD) curves using the following equation:

$$\text{Specific capacitance (F g}^{-1}) = \frac{I \times t_d}{m \times \Delta v} \quad (7)$$

where I is the constant discharge current (A), t_d is the discharge time (s), ΔV is the potential window during discharge (V), and m is the mass of the electroactive material in the electrode (g). These results highlight the superior energy storage performance of the heterojunction composite.

3.6 XPS

The XPS survey spectra (Fig. 7) display distinct signals corresponding to C 1s, O 1s, N 1s, Mn 2p, Bi 4f, and Ni 2p, confirming the successful formation and elemental composition of the BGN nanocomposite. The high-resolution Ni 2p spectrum exhibits characteristic $2p_{3/2}$ and $2p_{1/2}$ peaks at 854.11 and 871.58 eV, respectively. Peak deconvolution reveals the coexistence of Ni^{2+} species at 854.20 and 871.63 eV and Ni^{3+} species at 855.88 and 872.97 eV, indicating mixed-valence nickel states that can facilitate efficient interfacial charge transfer. The Mn 2p peaks at 641.37 and 653.12 eV correspond to Mn $2p_{1/2}$ and Mn $2p_{3/2}$ orbitals, suggesting redox-active behaviour of Mn centers capable of participating in electron-transfer processes during photocatalysis. The Bi 4f spectrum presents two well-defined peaks at 158.7 ($4f_{7/2}$) and 164.0 ($4f_{5/2}$) eV, consistent with the Bi^{3+} oxidation state in Bi–O bonding environments. The C 1s spectrum shows peaks at 284.6 eV (sp^2 C–C), 286.0 eV (C–O), and 286.4 eV (surface carbon). N 1s peaks at 398.3 and 399.9 eV are attributed to C–N=C and N–H groups in heptazine units, respectively. The O 1s spectrum reveals a main peak at 529.7 eV for metal–oxygen bonds and a secondary peak at 531.0 eV due to lattice oxygen.[54–57] These spectral features confirm strong chemical interaction and the presence of multiple oxidation states, which are beneficial for photocatalytic applications.

3.7 Theoretical analysis

In Fig. 8a–j, the DFT-derived HOMO–LUMO energy gaps (Table 3), obtained using molecular cluster models, are in the

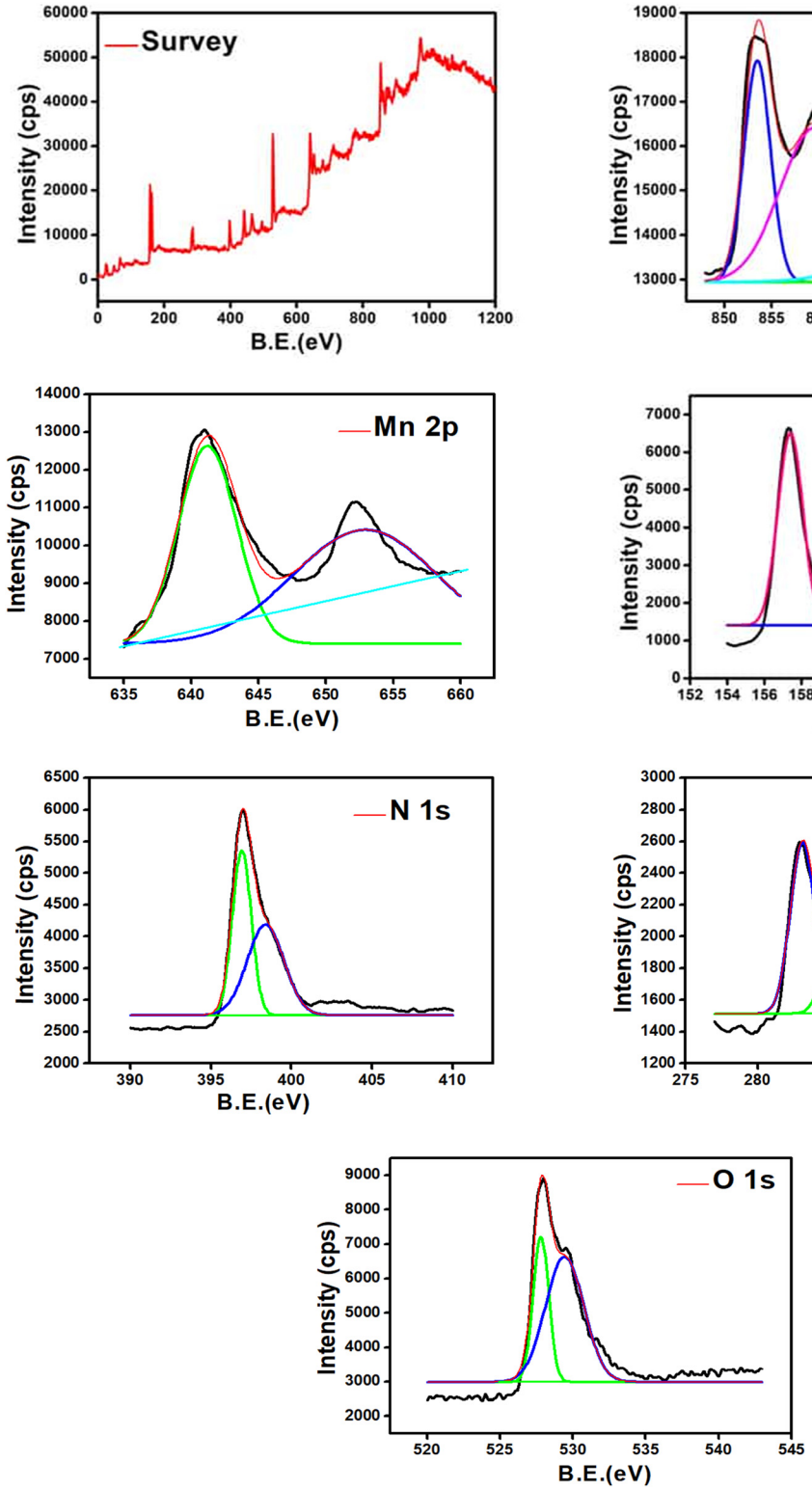

Fig. 7 XPS spectra of BGN materials: a survey spectrum of Ni 2p, Mn 2p, Bi 4f, C 1s, N 1s and O 1s.

same order of magnitude as the experimentally measured optical band gaps from UV-DRS (Table 2), with deviations of 0.2–0.3 eV for the individual oxides. Such differences are expected because cluster-based DFT describes localized electronic states and frontier orbital separations, whereas UV-DRS-derived band gaps reflect bulk solid state effects, including excitonic contributions, particle size, defects, and long-range periodicity. Moreover, the use of molecular models instead of

periodic boundary conditions introduces systematic shifts arising from finite-size effects and the choice of functional and basis set.

Despite these limitations, the cluster approach reliably captures relative trends in electronic structure and interfacial charge redistribution, which are most relevant for understanding charge-transfer processes in complex heterostructures. The very small HOMO–LUMO gap obtained for crystal violet (0.19 eV) originates from the highly delocalized π-electron system and the specific charge and multiplicity used in the molecular model. This value is not representative of a solid-state band gap and is intended only for qualitative comparison of charge-transfer propensity rather than quantitative evaluation.

Overall, the combined experimental and computational results consistently indicate that the Bi_2O_3/g-C_3N_4/$NiMnO_3$ heterostructure exhibits a reduced effective electronic gap (2.0 eV), enabling efficient visible-light absorption and supporting the proposed photocatalytic mechanism.

4. Photocatalytic study

When anionic (Congo red, CR) and cationic (crystal violet, CV) dyes are combined, donor–acceptor interactions can lead to the formation of a charge-transfer (CT) complex, producing a new absorption band rather than merely shifting the individual dye peaks. This new band, characteristic of supramolecular assembly or ground state complexation, is absent in the individual dyes.[52] The UV-vis absorption spectra of the individual dyes and their mixture are shown in Fig. 8c, while their chemical structures are presented in Fig. 9a and b.

4.1 Degradation of the mixed dye

The photocatalytic degradation efficiency of the synthesized photocatalysts was evaluated by monitoring the degradation rate of a mixed dye solution (crystal violet and Congo red) under natural sunlight irradiation. The photocatalytic activity of the synthesized nanocomposites was evaluated using a binary mixture of CV and CR (40 mg L^{-1} each) under natural sunlight irradiation at room temperature (27 °C) and neutral pH 6. For the mixed dye system (CV + CR), the photocatalytic experiments were performed at a total dye concentration of 40 ppm and a photocatalyst dosage of 0.6 g L^{-1} (60 mg), and the degradation efficiency was evaluated over a 90 min sunlight irradiation period. A fixed amount of photocatalyst (80 mg) was used in all experiments. Control tests without photocatalyst confirmed the high photostability of the dyes, with negligible degradation observed over 30 min under sunlight. The absorption spectra recorded during photocatalysis (Fig. 10a) show a gradual decrease in the characteristic peak at 530 nm, indicating simultaneous degradation of both dyes. Among the tested materials, the Bi_2O_3/g-C_3N_4/$NiMnO_3$ (BGN) ternary composite exhibited the highest photocatalytic efficiency (92%), outperforming $NiMnO_3$ (70.2%), Bi_2O_3 (79.5%), and g-C_3N_4 (88.7%). This enhanced performance is attributed to improved visible-light absorption, abundant reactive sites, efficient charge separation, and rapid interfacial charge transfer across the ternary heterojunction. Minimal dye removal in the dark confirmed that adsorption was negligible, and the observed

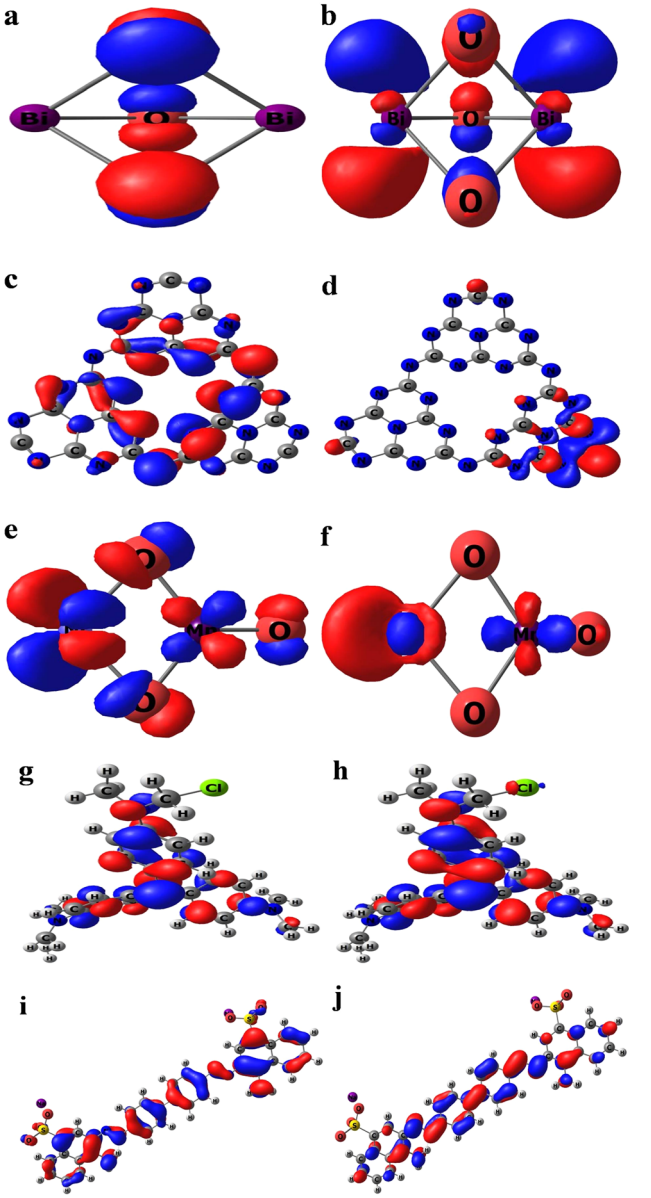

Fig. 8 Optimized molecular structures of (a) Bi_2O_3 (HOMO), (b) Bi_2O_3 (LUMO), (c) g-C_3N_4 (HOMO), (d) g-C_3N_4 (LUMO), (e) $NiMnO_3$ (HOMO), (f) $NiMnO_3$ (LUMO), (g) crystal violet (HOMO), (h) crystal violet (LUMO), (i) Congo red (HOMO) and (j) Congo red (LUMO).

Table 3 Data interpretation from DFT calculations

Specimen	E_{HOMO} (eV)	E_{LUMO} (eV)	ΔE_{gap}
Bi_2O_3	−5.3973	−2.7962	2.600937328
$NiMnO_3$	0.0378	2.0406	2.00277376
g-C_3N_4	−6.6424	−4.1672	2.475167136
Congo red	−5.0266	−2.3010	2.725513856
Crystal violet	−4.0550	−3.8620	0.192930244

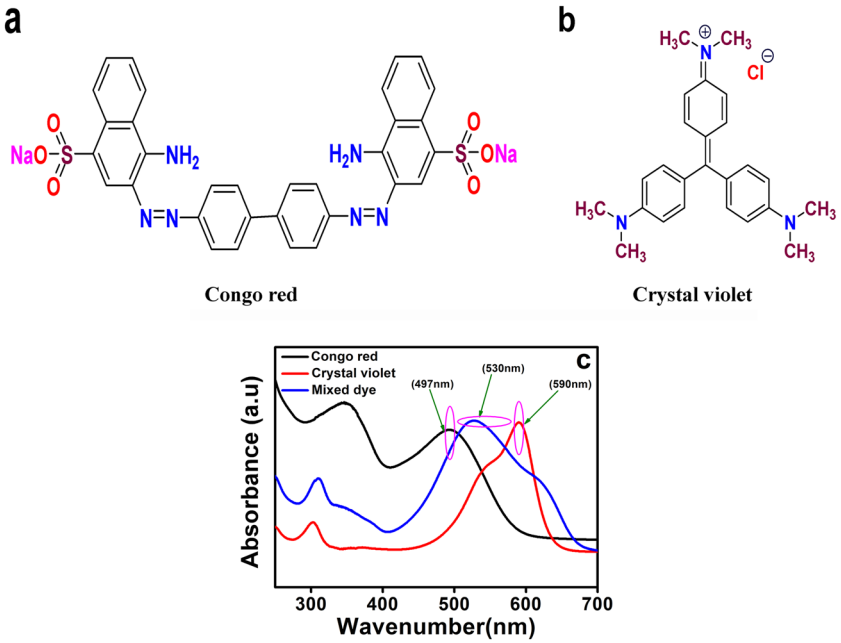

Fig. 9 Chemical structures of (a) Congo red and (b) crystal violet, and (c) UV-vis absorption spectra of the dyes.

photocatalytic activity was primarily due to reactive radicals ($^{\bullet}OH$ and $^{\bullet}O_2^-$) generated under light.

4.2 Kinetics, scavenger and reusability study

The photocatalytic degradation kinetics of Congo red (CR), crystal violet (CV) and mixed dyes by the synthesized samples were analyzed using the Langmuir–Hinshelwood kinetic model. The degradation behaviour was found to conform to a pseudo-first-order reaction mechanism. To better understand the kinetics of the process, the Langmuir–Hinshelwood model was applied using the equation:[58]

$$\ln(C/C_0) = k \times t \quad (8)$$

where C_0 and C are the initial and remaining dye concentrations and t is the time. The linear plots obtained from Fig. S3c, S4c, and Fig. 10c yielded the apparent rate constant (k), confirming that the ternary nanocomposite exhibits superior photocatalytic activity. This enhancement is attributed to enhanced light harvesting and efficient separation of charge carriers.

Fig. S3d, S4d, and Fig. 10d compare the degradation performance of various catalysts, clearly showing that the BGN composite outperformed both pristine and binary systems. To elucidate the reaction mechanism at the surface level, radical trapping experiments were conducted during dye degradation. Specific scavengers, namely isopropanol (IPA) for hydroxyl radicals ($^{\bullet}OH$), benzoquinone (BQ) for superoxide radicals ($^{\bullet}O_2^-$), and EDTA for photogenerated holes (h^+), were introduced into the reaction system.[59] The outcomes, shown in S3e, S4e, and Fig. 10e demonstrate that both hydroxyl and superoxide radicals play key roles in the degradation process, confirming that these reactive species significantly contribute to the overall photocatalytic activity of the ternary nanocomposites, thereby supporting the proposed heterojunction mechanism.

Reusability is a critical parameter for evaluating the practical applicability of photocatalysts in environmental remediation. The durability and recyclability of the BGN ternary nanocomposite were investigated by recovering the photocatalyst from Congo red (CR), crystal violet (CV), and mixed dye solutions after each photocatalytic cycle using a previously reported purification procedure. As shown in Fig. S3f, S4f, and Fig. 10f, the photocatalytic efficiency of BGN exhibited a gradual decrease over four successive cycles, while maintaining high degradation efficiency relative to the initial cycle. The slight decline in performance may be attributed to partial surface fouling by reaction intermediates and mild particle agglomeration during repeated use.

These findings confirm that the BGN ternary nanocomposites maintain high stability and reusability under prolonged photocatalytic conditions. Light alone had a significant effect, but the nanocomposites significantly reduced the dye concentration, and the photocatalytic efficiency ranked as: Bi_2O_3/g-C_3N_4/$NiMnO_3$ > g-C_3N_4 > Bi_2O_3 > $NiMNO_3$. A comparison was made between this work and previously reported ternary heterojunctions as shown in a tabular form in Table 4.

4.3 Photocatalytic degradation mechanism

Under solar light irradiation, the Bi_2O_3/g-C_3N_4/$NiMnO_3$ (BGN) ternary heterojunction is effectively photoactivated due to its well-aligned band structure and enhanced visible-light absorption capability. Upon illumination, all three semiconductor components absorb incident photons ($h\nu$), generating electron–hole pairs by promoting electrons (e^-) from their valence bands (VB) to the conduction bands (CB), and leaving holes (h^+) behind in the VB:

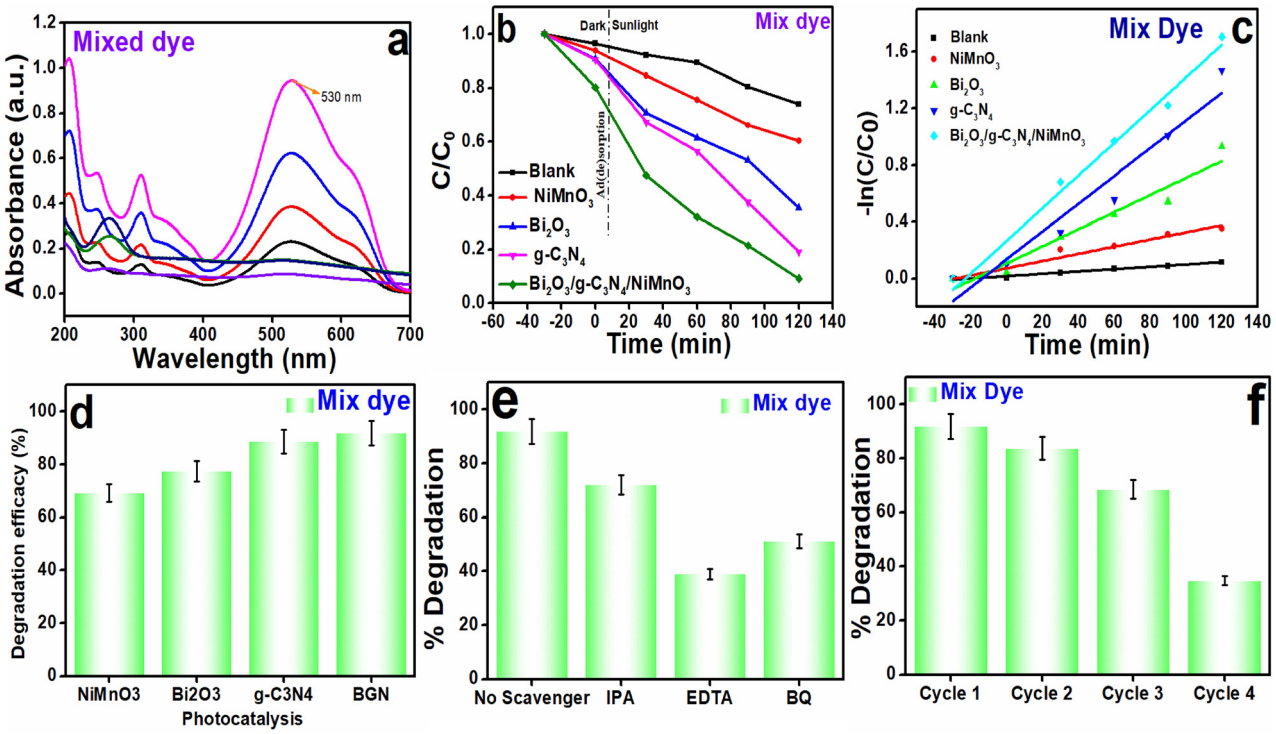

Fig. 10 UV-Visible absorption analysis of the photocatalytic activity of the Bi_2O_3/g-C_3N_4/$NiMnO_3$ ternary nanocomposites for a binary mixed dye (Congo red and crystal violet): (a) absorption spectra under visible light, (b) C/C_0 *vs.* time plot, (c) pseudo-first-order kinetic fit, (d) degradation efficiency, (e) scavenger study revealing active species, and (f) recyclability over multiple cycles.

$$Bi_2O_3/g\text{-}C_3N_4/NiMnO_3 + h\nu \rightarrow e^- + h^+ \quad (9)$$

At the interface, electrons in the CBs of $NiMnO_3$ (+0.5 V) and Bi_2O_3 (+0.3 V) recombine with holes in the VB of g-C_3N_4 (+1.6 V), following an S-scheme mechanism:

$$e^-_{NiMnO_3/Bi_2O_3} + h_{g\text{-}C_3N_3}{}^+ \rightarrow \text{recombination} \quad (10)$$

This selective recombination preserves the highly reducing electrons in the CB of g-C_3N_4 (−1.1 V) and the strongly oxidizing holes in the VB of Bi_2O_3 (+2.6 V). The g-C_3N_4 CB electrons efficiently reduce O_2 to superoxide radicals, since −1.1 V is more negative than the $O_2/{}^\bullet O_2^-$ potential (−0.33 V):

$$e^- + O_2 \rightarrow {}^\bullet O_2^- \quad (11)$$

Meanwhile, the Bi_2O_3 VB holes (+2.6 V) oxidize OH^-/H_2O to hydroxyl radicals, as the potential is more positive than the $OH^-/{}^\bullet OH$ level (+2.38 V):

$$h^+ + OH^-/H_2O \rightarrow {}^\bullet OH + H^+ \quad (12)$$

Table 4 Comparative overview of photocatalytic performance based on synthesis methods, light sources, and degradation efficiencies

Sl. no.	Photo-catalysis	Synthesis method	Time (min)	Pollutants	Light source	%*D* efficiency	Ref.
1	RGO/γ-Fe_2O_3/ZnO	Microwave synthesis	12, 21, 21	Malachite green (MG), methyl orange (MO), rhodamine B (RhB)	UV irradiation	100	60
2	$SrTiO_3$/TiO_2/Cu_2O	Reflux method	120	Methylene blue (MB), rhodamine B (RhB), methyl orange (MO)	LED light source (λ > 400 nm, intensity 46.1 W cm^{-2}	85	61
3	NiO/Ag/TiO_2	Deposition coprecipitation	60	Methylene blue (MB)	Sunlight	93.15	62
4	V_2O_5–Fe_3O_4/rGO	One-pot solvothermal process	100, 110	Methylene blue (MB)	UV/visible light	89.2 and 76	63
5	$ZnFe_2O_4$/Fe_2O_3/chitosan	Sol–gel method	120	Eosin (EO) and erythrosine (ER)	Osram lamp (400 W)	84.2 and 96.5	64
6	RGO/γ-Fe_2O_3/ZnO	Rapid microwave irradiation route	21	Malachite green (MG), methyl orange (MO), rhodamine B (RhB)	UV irradiation	100	65
7	MoS_2–NiO–CuO	Hydrothermal process	80, 100	Crystal violet (CV), methyl orange (MO)	UV-Visible light irradiation	95 and 93	66
8	This study	Precipitation	90	Congo red (CR), CV (crystal violet), binary mix	Sunlight	94, 99 and 91	—

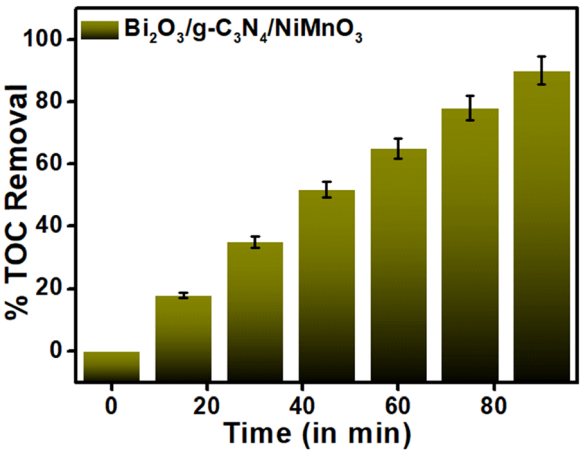

Fig. 11 TOC removal of mixed dyes under solar light using the Bi_2O_3/g-C_3N_4/$NiMnO_3$ photocatalyst.

These reactive oxygen species ($^{\bullet}O_2^-$ and $^{\bullet}OH$) synergistically degrade both cationic (crystal violet) and anionic (Congo red) dye pollutants through oxidative cleavage, hydrogen abstraction, and ring-opening, ultimately leading to complete mineralization:

$$^{\bullet}O_2^-/^{\bullet}OH + \text{crystal violet (CV) or Congo red (CR)} \rightarrow CO_2 + H_2O + \text{intermediates} \quad (13)$$

Furthermore, the progressive decrease in total organic carbon (TOC) with irradiation time (Fig. 11) provides direct evidence of effective mineralization rather than mere dye decolourization. As shown in Fig. 11, TOC removal increases steadily, reaching nearly 90% after prolonged solar irradiation, indicating continuous oxidation of intermediate organic fragments into inorganic end products. The slightly slower TOC removal compared to UV-vis decolourization confirms the stepwise degradation pathway, wherein complex dye molecules are first transformed into smaller intermediates before complete mineralization. The intimate interfacial contact among Bi_2O_3, g-C_3N_4, and $NiMnO_3$, together with the built-in electric field of the S-scheme heterojunction, ensures efficient charge separation and sustained generation of $^{\bullet}OH$ and $^{\bullet}O_2^-$ radicals, ultimately accounting for the high photocatalytic efficiency and mineralization capability of the BGN system under visible-light irradiation (Scheme 2).

5. Conclusion

In this study, Bi_2O_3/g-C_3N_4/$NiMnO_3$ (BGN) ternary nanocomposites were successfully fabricated *via* a facile precipitation strategy and applied for the visible-light-driven degradation of individual (Congo red and crystal violet) as well as mixed organic dyes. Comprehensive physicochemical and optical characterizations confirmed the formation of an integrated heterostructure, with high-resolution TEM revealing intimate interfacial contact among the constituent phases, indicative of strong electronic coupling. Electrochemical investigations, including EIS (electrochemical impedance spectroscopy) and CV (cyclic voltammetry), provided insights into the enhanced charge transfer kinetics and redox activity of the photocatalyst, affirming its superior interfacial conductivity and electrochemical responsiveness. The optimized nanocomposite exhibited remarkable photocatalytic efficiency, durability, and recyclability under visible-light irradiation. Notably, the generation of reactive oxygen species, primarily hydroxyl ($^{\bullet}OH$) and superoxide ($O_2^{\bullet-}$) radicals, was found to be the dominant pathway for dye decomposition, leading to complete mineralization. Stability assessments over multiple photocatalytic cycles confirmed the structural integrity and reusability of the catalyst. Overall, the BGN ternary heterojunction emerges as a

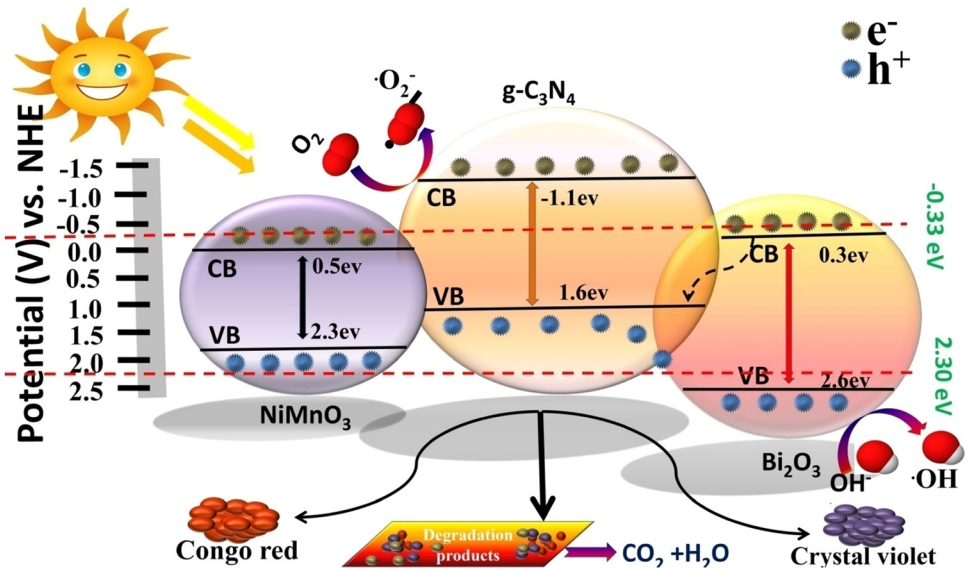

Scheme 2 Proposed S-scheme charge transfer mechanism in Bi_2O_3/g-C_3N_4/$NiMnO_3$ under visible light, promoting efficient dye degradation (Congo red, crystal violet) *via* reactive oxygen species ($^{\bullet}O_2^-$, $^{\bullet}OH$).

promising candidate for sustainable wastewater remediation owing to its synergistically enhanced photocatalytic activity and operational robustness.

Bi_2O_3/g-C_3N_4/$NiMnO_3$ nanocomposites demonstrate strong potential for wastewater treatment, but key challenges remain for real-world use. Long-term stability under varying conditions, green and scalable synthesis methods, and deeper mechanistic understanding *via in situ* spectroscopy are crucial. Enhancing the heterojunction *via* doping or surface modifications could boost visible-light performance. Finally, integrating these materials into continuous-flow systems will be vital for industrial applications. Continued innovation in design, mechanisms, and integration is essential for sustainable environmental remediation.

Although conventional synthesis and characterization techniques were employed, their combined use with experimental–theoretical analysis provides new insight into the structure–property–performance relationship of the Bi_2O_3/g-C_3N_4/$NiMnO_3$ ternary system.

Author contributions

Rasmirekha Pattanaik: investigation, methodology, formal analysis, data curation, visualization, and writing – original draft. Rishabh Kamal and Debapriya Pradhan: investigation, resources, and writing – review and editing. Suresh Kumar Dash: conceptualization, methodology, supervision, writing – review and editing, resources, and funding acquisition.

Conflicts of interest

The authors declare that they have no competing financial interests or personal relationships that could have affected the objectivity or integrity of the work reported in this article.

Data availability

All data supporting the findings of this study are included within the main article and its supplementary information (SI). The supplementary information file includes detailed data on BET surface area, PL spectroscopy, Raman spectroscopy, and individual dye degradation experiments. See DOI: https://doi.org/10.1039/d6nj00220j.

No computational code was used in this study. Additional data can be provided by the corresponding author upon reasonable request.

Acknowledgements

We are indebted to Prof. Jagdish Kumar, Prof. in Physics, Delhi University, Delhi, for his contribution toward the DFT analysis and DFT energy images of the synthesized samples. The authors gratefully acknowledge the Department of Chemistry, ITER, Siksha 'O' Anusandhan (Deemed to be University), Bhubaneswar, for providing laboratory facilities essential to this work. We also extend our sincere thanks to the research centre at Kalinga Institute of Industrial Technology and the National Institute of Technology Rourkela for access to their analytical instrumentation and technical support.

References

1 P. K. Panda, R. Pattanaik, S. Mishra, D. Pradhan and S. Kumar Dash, *Mater. Today: Proc.*, 2023, **80**, 2214–7853, DOI: 10.1016/j.matpr.2023.11.039.
2 Z. Wu, X. Chen, X. Liu, X. Yang and Y. Yang, *Nanoscale Res. Lett.*, 2019, **14**, 147.
3 R. Pattanaik, D. Pradhan and S. K. Dash, *Curr. Nanosci.*, 2024, **21**, 201–217.
4 S. Y. Lee, D. Kang, S. Jeong, H. T. Do and J. H. Kim, *ACS Omega*, 2020, **5**, 4233–4241.
5 V. Batra, I. Kaur, D. Pathania, S. Sonu and V. Chaudhary, *Appl. Surf. Sci. Adv.*, 2022, **11**, 100314.
6 H. Dong, G. Chen, J. Sun, C. Li, Y. Yu and D. Chen, *Appl. Catal., B*, 2013, **134–135**, 46–54.
7 D. S. Pattanayak, M. Surana, A. Kumar, D. Singh and D. Pal, *Sustainable Chem. Environ.*, 2024, **7**, 100141.
8 X. Liu, L. Pan, T. Lv, Z. Sun and C. Q. Sun, *J. Colloid Interface Sci.*, 2013, **408**, 145–150.
9 D. Nayak, A. Kumar and R. Thangavel, *ACS Appl. Nano Mater.*, 2023, **6**, 19476–19490.
10 D. Pradhan, S. K. Biswal, R. Pattanaik, N. Nayak and S. K. Dash, *New J. Chem.*, 2024, **48**, 16853–16868.
11 P. Basumatary, R. Basumatary, D. Konwar and A. Ramchiary, *Surf. Interfaces*, 2025, **62**, 106148.
12 R. Pattanaik, R. Kamal, D. Pradhan and S. K. Dash, *Discover Appl. Sci.*, 2025, **7**, 685.
13 S. Upadhyay, I. Assadullah and R. Tomar, *Sci. Rep.*, 2024, **14**, 7415.
14 M. Imtiaz, R. Y. Khosa, L. A. El Maati, S. Aman, A. G. Al-Sehemi, A. M. A. Henaish and T. A. M. Taha, *Optik*, 2024, **300**, 171639.
15 S. Swathi, R. Yuvakkumar, G. Ravi, A. G. Al-Sehemi and D. Velauthapillai, *Nanoscale Adv.*, 2022, **4**, 2501–2508.
16 O. Rosales-González, F. Sánchez-De Jesús, M. A. Camacho-González, C. A. Cortés-Escobedo and A. M. Bolarín-Miró, *Mater. Sci. Eng. B*, 2020, **261**, 114773.
17 K. Chandiran, M. S. Pandian, S. Balakrishnan, S. Pitchaimuthu, Y.-S. Chen and K. C. Nagamuthu Raja, *Colloids Surf., A*, 2024, **692**, 133888.
18 P. B. Koli, S. G. Shinde, K. H. Kapadnis, A. P. Patil, M. P. Shinde, S. D. Khairnar, D. B. Sonawane and R. S. Ingale, *J. Indian Chem. Soc.*, 2021, **98**, 100225.
19 F. Poorsajadi, M. H. Sayadi, M. Hajiani and M. R. Rezaei, *Int. J. Environ. Anal. Chem.*, 2022, **102**, 7165–7178.
20 M. Ahmaruzzaman and S. R. Mishra, *Mater. Res. Bull.*, 2021, **143**, 111417.
21 D. Alhashmialameer, S. Aman, M. Abdullah, R. Y. Khosa, S. Manzor, H. M. Ali, M. H. Helal, H. M. T. Farid, M. S. Waheed and T. A. Taha, *J. Sol-Gel Sci. Technol.*, 2023, **105**, 85–97.

22 D. Mehandjiev, A. Naydenov and G. Ivanov, *Appl. Catal., A*, 2001, **206**, 13–18.
23 S. Karmakar and D. Behera, *Ceram. Int.*, 2019, **45**, 13052–13066.
24 H.-Y. Kim, J. Shin, I.-C. Jang and Y.-W. Ju, *Energies*, 2019, **13**, 36.
25 S. Qiao, N. Huang, Y. Sun, J. Zhang, Y. Zhang and Z. Gao, *J. Alloys Compd.*, 2019, **775**, 1109–1116.
26 V. Jose, V. Jose, E. Kuruvilla, M. Arunkumar, A. Segar Deepi, G. Srikesh and A. Samson Nesaraj, *Inorg. Chem. Commun.*, 2023, **156**, 111205.
27 K. Chandiran, M. S. Pandian, S. Balakrishnan, S. Pitchaimuthu, Y.-S. Chen and K. C. Nagamuthu Raja, *Colloids Surf., A*, 2024, **692**, 133888.
28 K. Chandiran and K. C. Nagamuthu Raja, *Colloids Surf., A*, 2023, **667**, 131434.
29 S. Swathi, R. Yuvakkumar, G. Ravi, A. G. Al-Sehemi and D. Velauthapillai, *Nanoscale Adv.*, 2022, **4**, 2501–2508.
30 Z. Li, X. Tang, G. Huang, X. Luo, D. He, Q. Peng, J. Huang, M. Ao and K. Liu, *Sep. Purif. Technol.*, 2020, **242**, 116825.
31 L. Mohanty, D. Sundar Pattanayak, R. Singhal, D. Pradhan and S. Kumar Dash, *Inorg. Chem. Commun.*, 2022, **138**, 109286.
32 Q. Zhuang, B. Wu, H. Wang, X. Wu, P. Xu, H. Yi, Z. Xiong, G. Shi, Q. Wang and B. Wang, *Ionics*, 2021, **27**, 4811–4818.
33 S. Swathi, R. Yuvakkumar, G. Ravi, A. G. Al-Sehemi and D. Velauthapillai, *Nanoscale Adv.*, 2022, **4**, 2501–2508.
34 S. Chandel, S. Lee, S. Kim, S. P. Singh, J. Gim, J. Kim and A. K. Rai, *New J. Chem.*, 2019, **43**, 12916–12922.
35 F. Akram, M. Saeed, J. Akhtar, S. A. Raza Naqvi and A. U. Haq, *Z. Phys. Chem.*, 2021, **235**, 1609–1627.
36 L. P. Dias, F. C. Correia, J. M. Ribeiro and C. J. Tavares, *Coatings*, 2020, **10**, 445.
37 Y. Che, Q. Liu, B. Lu, J. Zhai, K. Wang and Z. Liu, *Sci. Rep.*, 2020, **10**, 721.
38 D. Pradhan, L. Mohanty, R. Singhal, E. Falletta and S. K. Dash, *Inorg. Chem. Commun.*, 2023, **156**, 111259.
39 G. Divya, S. Sivakumar, D. Sakthi, A. Priyadharsan, V. Arun, R. Kavitha and S. Boobas, *J. Inorg. Organomet. Polym. Mater.*, 2021, **31**, 4480–4490.
40 N. Boonprakob, D. Channei and C. Zhao, *Discover Nano*, 2024, **19**, 22.
41 S. Upadhyay, I. Assadullah and R. Tomar, *Sci. Rep.*, 2024, **14**, 7415.
42 T. Li, S. Quan, X. Shi, L. Yang and C. Liu, *Catal. Lett.*, 2020, **150**, 640–651.
43 L. Mohanty, D. S. Pattanayak, D. Pradhan and S. K. Dash, *Environ. Qual. Manage.*, 2022, **32**, 45–59.
44 S. Noor, S. Sajjad, S. A. K. Leghari, I. Ahmad and T. Mahmood, *Mater. Res. Express*, 2020, **6**, 1250d8.
45 D. Hong, Y. Yamada, A. Nomura and S. Fukuzumi, *Phys. Chem. Chem. Phys.*, 2013, **15**, 19125.
46 L. Ranganatha V., G. S. Shivaganga, S. Pramila, G. Nagaraju, P. Parameswara, Abdel-Basit Al-Odayni, Abdulla A. Al-Kahtani and C. Mallikarjunaswamy, *Ionics*, 2025, **31**, 3537–3550.
47 H. Mirhosseini, A. Mostafavi, T. Shamspur and G. Sargazi, *J. Mater. Sci.: Mater. Electron.*, 2020, **31**, 17903–17920.
48 S. Tonda, S. Kumar, Y. Gawli, M. Bhardwaj and S. Ogale, *Int. J. Hydrogen Energy*, 2017, **42**, 5971–5984.
49 K. Chandiran and K. C. Nagamuthu Raja, *Colloids Surf., A*, 2023, **667**, 131434.
50 D. Pradhan, S. K. Biswal, N. Nayak, R. Singhal, S. K. Beriha, R. Pattanaik and S. K. Dash, *ChemistrySelect*, 2024, **9**, e202403211.
51 A. C. Lazanas and M. I. Prodromidis, *ACS Meas. Sci. Au*, 2023, **3**, 162–193.
52 G. Richhariya and A. Kumar, *Opt. Mater.*, 2018, **79**, 296–301.
53 D. Alhashmialameer, S. Aman, M. Abdullah, R. Y. Khosa, S. Manzor, H. M. Ali, M. H. Helal, H. M. T. Farid, M. S. Waheed and T. A. Taha, *J. Sol-Gel Sci. Technol.*, 2022, **105**, 85–97.
54 S. Zhao, H. Li, Z. Jian, Y. Xing and S. Zhang, *RSC Adv.*, 2018, **8**, 41749–41755.
55 S. Qiao, N. Huang, J. Zhang, Y. Zhang, Y. Sun and Z. Gao, *J. Solid State Electrochem.*, 2019, **23**, 63–72.
56 M. Jiang, Y. Ding, H. Zhang, J. Ren, J. Li, C. Wan, Y. Hong, M. Qi, B. Mei, L. Deng, Y. Wu, T. Han, H. Zhang and J. Liu, *J. Solid State Electrochem.*, 2020, **24**, 2487–2497.
57 L. Chen, S. Yang, W. Qi, Q. Zhang, J. Zhu and P. Zhao, *ACS Appl. Mater. Interfaces*, 2021, **13**, 49993–50004.
58 R. Pattanaik, R. Kamal, D. Pradhan and S. K. Dash, *J. Met., Mater. Miner.*, 2025, **35**, e2228.
59 R. Pattanaik, D. Pradhan, R. Kamal and S. K. Dash, *Next Mater.*, 2025, **8**, 100847.
60 P. Yadav, S. Manori, P. Chamoli and R. Kumar Shukla, *Inorg. Chem. Commun.*, 2024, **167**, 112791.
61 P. Basumatary, R. Basumatary, D. Konwar and A. Ramchiary, *Surf. Interfaces*, 2025, **62**, 106148.
62 W. Mohammed, M. Matalkeh, R. M. Al Soubaihi, A. Elzatahry and K. M. Saoud, *ACS Omega*, 2023, **8**, 40063–40077.
63 F. Jafari and F. R. Rahsepar, *ACS Omega*, 2023, **8**, 35427–35439.
64 S. A. Ehsanizadeh, M. Ahmadi-Kashani, M. Salavati-Niasari, F. H. Alsultany and H. H. Hamza, *Appl. Water Sci.*, 2025, **15**, 144.
65 P. Yadav, S. Manori, P. Chamoli and R. Kumar Shukla, *Inorg. Chem. Commun.*, 2024, **167**, 112791.
66 K. Dharmalingam, A. K. Bojarajan, R. Gopal, E. Thangavel, S. A. B. A. Omari and S. Sangaraju, *Sci. Rep.*, 2024, **14**, 14518.

